Research Papers

GREENSUSMATER

Greensusmater
Vol. 3, No. 1, 2026
https://doi.org/10.62755/gsm.2026.02
Check for updates

Electrospun PAN/PVP/ZnO Nanofiber Membrane As A Photocatalyst For Methylene Blue Degradation Under UV Irradiation

Rut Rabekka Gultom[1], Istiara Rizqillah Hanifah[1], Rizky Aflaha[2], Hannah Faye M. Austria[3], T. M. Subrahmanya[4], Januar Widakdo[5], Aditya Rianjanu[1,*]

[1] *Department of Materials Engineering, Faculty of Industrial Technology, Institut Teknologi Sumatera, Terusan Ryacudu, Way Hui, Jati Agung, Lampung Selatan 35365, Indonesia*
[2] *Department of Physics, Faculty of Mathematics and Natural Sciences, Universitas Gadjah Mada, Sekip Utara PO Box BLS 21, Yogyakarta 55281, Indonesia*
[3] *Graduate Institute of Environmental Engineering, National Taiwan University, Taipei 10617, Taiwan*
[4] *Advanced Membrane Materials Research Center, Graduate Institute of Applied Science and Technology, National Taiwan University of Science and Technology, Taipei 10607, Taiwan*
[5] *Department of Physics, Faculty of Mathematics and Natural Sciences, Universitas Indonesia, Depok 16424, Indonesia*

Corresponding author: aditya.rianjanu@mt.itera.ac.id

ARTICLE HISTORY: Received: March 19, 2026 | Revised: May 1, 2026 | Accepted: May 3, 2026

ABSTRACT

Textile dye pollution remains a critical environmental concern, necessitating the development of efficient and recoverable photocatalysts for wastewater remediation. In this study, polyacrylonitrile/polyvinylpyrrolidone/zinc oxide (PAN/PVP/ZnO) nanofiber membranes were fabricated via electrospinning with varying ZnO loadings (0, 0.5, 1, and 2 mmol) and evaluated for the photocatalytic degradation of methylene blue (MB) under ultraviolet (UV) irradiation. Scanning electron microscopy (SEM) revealed continuous, bead-free nanofibers with mean diameters of 355–552 nm, and energy dispersive X-ray spectroscopy (EDS) confirmed systematic Zn incorporation up to 34.52 wt%. A comparative study demonstrated that heat treatment at 450 ℃ was essential for converting the $Zn(NO_3)_2$ precursor into the photocatalytically active ZnO phase. X-ray diffraction (XRD) and Fourier-transform infrared spectroscopy (FTIR) confirmed the retention of the polymer matrix integrity. Among the tested formulations, PAN/PVP/ZnO-1 (1 mmol) exhibited the highest photocatalytic performance, achieving approximately 95% MB degradation within 180 min, with a pseudo-first-order rate constant of $k = 0.0251\ min^{-1}$ ($R^2 = 0.9926$), approximately 9 times faster than the neat PAN/PVP membrane. Higher ZnO loading (2 mmol) resulted in reduced photocatalytic performance. These findings indicate that 1 mmol ZnO is the optimal loading for PAN/PVP nanofiber photocatalysts, offering a promising recoverable membrane system for photocatalytic dye removal from wastewater.

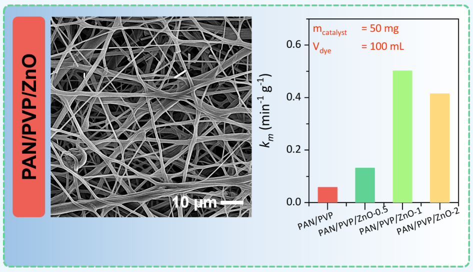

Keywords: *electrospinning; PAN/PVP/ZnO nanofiber; photocatalysis; methylene blue degradation; wastewater treatment*

1. INTRODUCTION

The rapid expansion of the global textile industry has led to the discharge of large volumes of dye-containing wastewater into aquatic ecosystems, posing severe environmental and public health risks [1,2]. Among synthetic dyes, methylene blue (MB) is a widely used cationic thiazine dye employed in textile dyeing, pharmaceutical formulations, and biological staining [3]. Conventional wastewater treatment approaches, including coagulation–flocculation, adsorption, and biological degradation, often suffer from incomplete dye removal, generation of secondary pollutants, and high operational costs, underscoring the urgent need for more efficient and sustainable remediation technologies [4,5,6].

Heterogeneous photocatalysis has emerged as a highly promising advanced oxidation process (AOP) for the degradation of recalcitrant organic pollutants in aqueous systems [7,8]. In this process, semiconductor photocatalysts generate reactive oxygen species (ROS), such as hydroxyl radicals (•OH) and superoxide anions ($•O_2^-$), upon light irradiation, which can achieve complete mineralization of organic dyes into CO_2, H_2O, and inorganic ions without producing secondary pollution [8,9]. Among various semiconductor photocatalysts (TiO_2, WO_3, g-C_3N_4), zinc oxide (ZnO) has attracted considerable attention owing to its wide bandgap (~3.37 eV), high electron mobility, strong ultraviolet absorption, low cost, and environmental compatibility [10,11,12]. However, the practical application of ZnO in powder form is severely limited by the difficulty of post-treatment recovery from treated water, nanoparticle aggregation that reduces active surface area, and the risk of secondary contamination [13,14]. To overcome these challenges, immobilizing ZnO onto polymeric nanofiber supports fabricated via electrospinning has been recognized as an effective strategy, as electrospun nanofibers offer an exceptionally high surface-area-to-volume ratio, interconnected porous structure for enhanced pollutant accessibility, and a membrane form factor that enables straightforward catalyst recovery [15,16].

In this context, polyacrylonitrile (PAN) and polyvinylpyrrolidone (PVP) represent a synergistic bi-

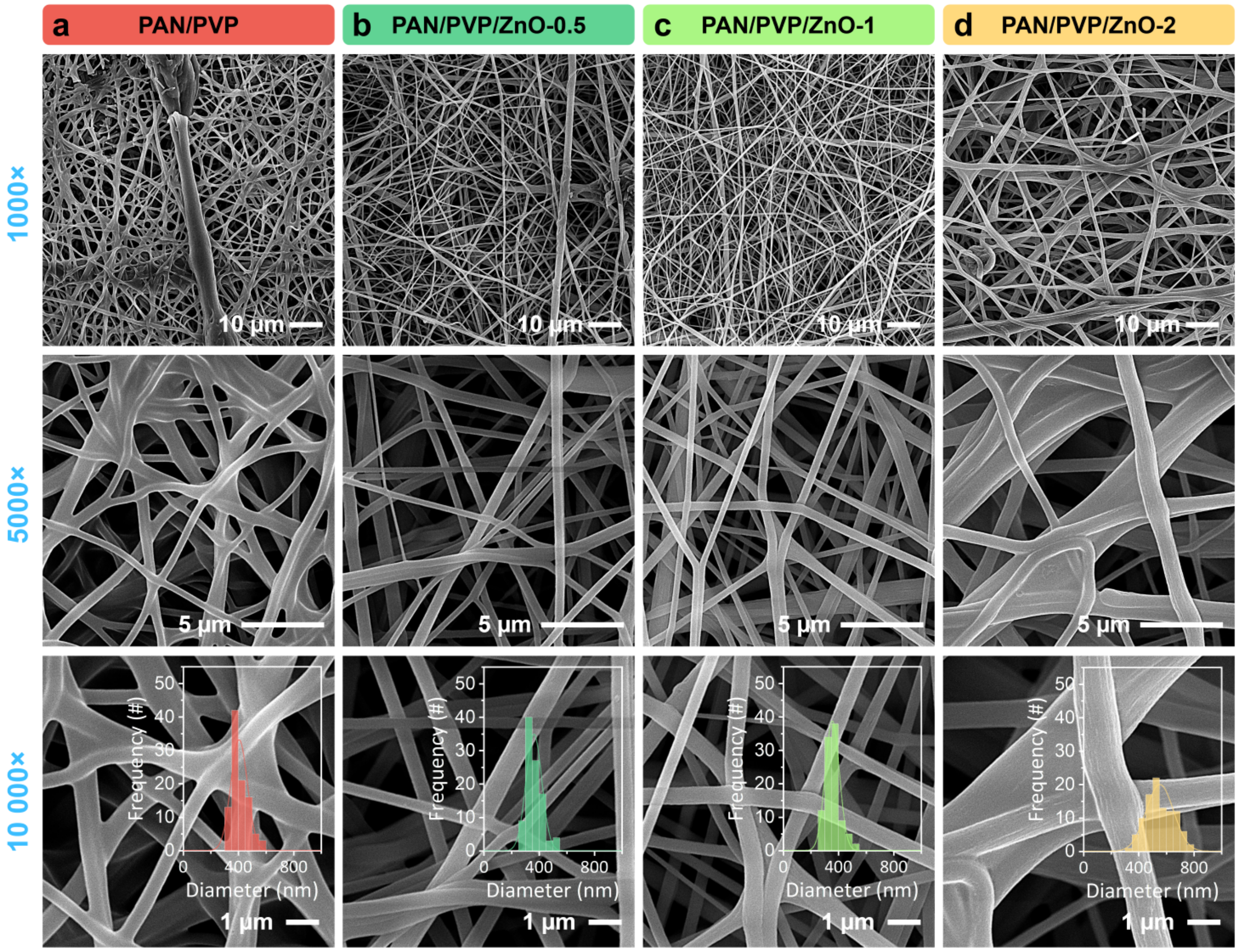

Figure 1. SEM micrographs of electrospun nanofiber membranes at magnifications of 1000× (top row), 5000× (middle row), and 10,000× (bottom row): (a) PAN/PVP, (b) PAN/PVP/ZnO-0.5, (c) PAN/PVP/ZnO-1, and (d) PAN/PVP/ZnO-2. Insets in the bottom row show the corresponding fiber diameter distribution histograms measured from 100 fibers using ImageJ software.

nary polymer blend for nanofiber-based photocatalyst supports: PAN provides excellent mechanical strength, chemical stability, and superior electrospinnability, while PVP enhances surface hydrophilicity and functions as a stabilizing agent for uniform ZnO dispersion within the fiber matrix [17]. Although previous studies have explored PAN/ZnO and PVP/ZnO nanofiber systems individually for photocatalytic applications [18,19], limited work has investigated the combined PAN/PVP binary blend with systematically varied ZnO loadings for dye photodegradation. In the present study, PAN/PVP/ZnO nanofiber membranes were fabricated via electrospinning with varying ZnO loadings (0, 0.5, 1, and 2 mmol) and subsequently heat-treated at 450 °C to convert the zinc precursor into the photocatalytically active ZnO phase. The resulting membranes were comprehensively characterized by scanning electron microscopy (SEM), energy dispersive X-ray spectroscopy (EDS), X-ray diffraction (XRD), and Fourier-transform infrared spectroscopy (FTIR), and their photocatalytic performance was evaluated for methylene blue degradation under ultraviolet irradiation. The objective of this work is to determine the optimal ZnO loading that maximizes photocatalytic efficiency while maintaining the structural integrity of the nanofiber membrane, thereby advancing the development of recoverable nanofiber-based photocatalysts for wastewater treatment.

2. MATERIALS AND METHODS

2.1 Materials

Polyacrylonitrile (PAN, Mw = 150,000 g/mol) and polyvinylpyrrolidone (PVP, Mw ≈ 1,300,000 by light scattering) were obtained from Sigma-Aldrich (Singapore). Zinc nitrate hexahydrate ($Zn(NO_3)_2{\cdot}6H_2O$, 98%) was purchased from Sigma-Aldrich (Singapore) and served as the zinc precursor for in-situ ZnO formation. N,N-Dimethylformamide (DMF, Merck, Germany) was used as the solvent. Methylene blue (MB, C.I. 52,015, Merck, Germany) was used as a model organic pollutant. Deionized water was used throughout all experiments. All chemicals were used as received without further purification.

2.2 Preparation of PAN/PVP/ZnO nanofibers

PAN/PVP/ZnO nanofiber membranes were fabricated via the electrospinning technique combined with subsequent heat treatment. First, predetermined amounts of $Zn(NO_3)_2{\cdot}6H_2O$ (0, 0.148, 0.297, and 0.595 g, corresponding to 0, 0.5, 1, and 2 mmol, respectively) were dissolved in

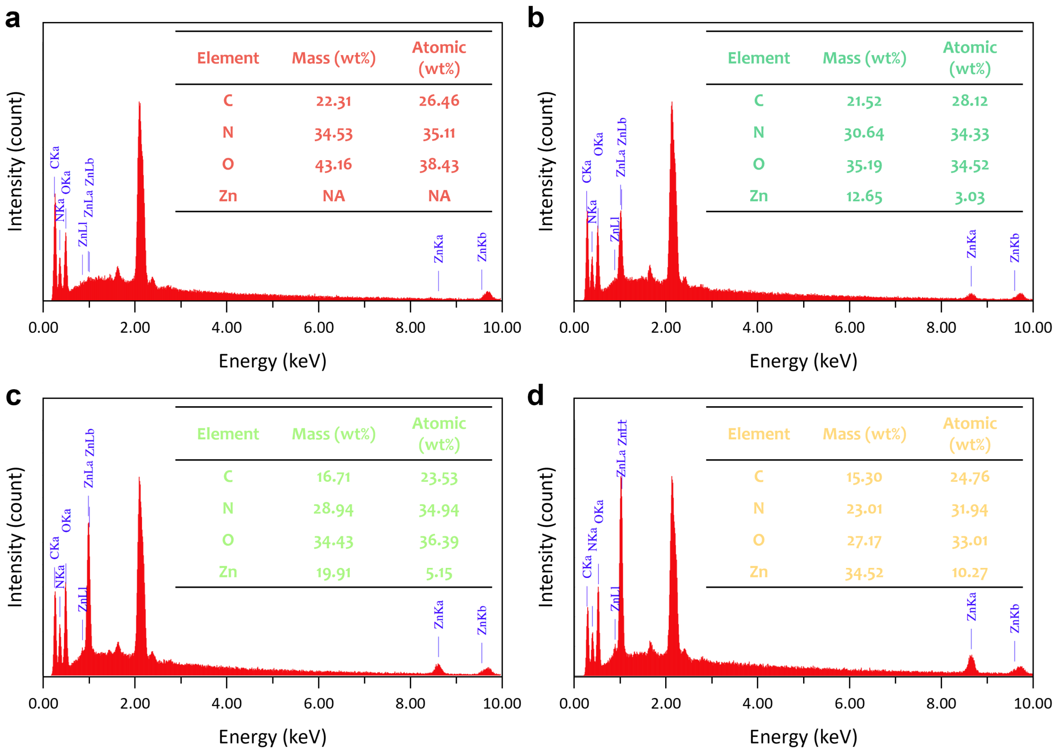

a

Element	Mass (wt%)	Atomic (wt%)
C	22.31	26.46
N	34.53	35.11
O	43.16	38.43
Zn	NA	NA

b

Element	Mass (wt%)	Atomic (wt%)
C	21.52	28.12
N	30.64	34.33
O	35.19	34.52
Zn	12.65	3.03

c

Element	Mass (wt%)	Atomic (wt%)
C	16.71	23.53
N	28.94	34.94
O	34.43	36.39
Zn	19.91	5.15

d

Element	Mass (wt%)	Atomic (wt%)
C	15.30	24.76
N	23.01	31.94
O	27.17	33.01
Zn	34.52	10.27

Figure 2. EDS spectra and elemental composition of electrospun nanofiber membranes: (a) PAN/PVP, (b) PAN/PVP/ZnO-0.5, (c) PAN/PVP/ZnO-1, and (d) PAN/PVP/ZnO-2. Inset tables show the quantitative elemental composition in weight percent (wt%) and atomic percent (at%).

10 mL of DMF under magnetic stirring at 600 rpm for 30 min until a homogeneous solution was obtained. After complete dissolution, 0.8 g of PAN and 0.5 g of PVP were added into the zinc nitrate/DMF solution, and the temperature was raised to 60 °C under continuous stirring until the polymers were fully dissolved. The resulting solution was then allowed to cool naturally to room temperature before use.

The prepared solution was transferred into a 10 mL Terumo plastic syringe fitted with a 21-gauge stainless-steel needle. Electrospinning was carried out on a digital spinning platform (ILMI-N101, Integrated Laboratory of Materials and Instrumentation, Bandung, Indonesia) under the following fixed parameters: applied voltage 9 kV, feed rate 0.5 mL/h, and needle-to-collector distance 12 cm. The nanofibers were deposited onto a rotating drum collector covered with aluminum foil. All spinning was conducted at ambient temperature and humidity. The electrospinning process continued until the solution was completely consumed, typically requiring approximately 20 h.

The as-spun nanofiber membranes were subsequently subjected to heat treatment in a tube furnace under nitrogen (N_2) atmosphere. The temperature was raised to 450 °C at a heating rate of 3 °C/min and held for 1 h to thermally decompose the zinc nitrate precursor into ZnO within the nanofiber matrix. The heat-treated membranes were allowed to cool naturally to room temperature inside the furnace. Five sample types were prepared and designated as PAN/PVP (0 mmol, control), PAN/PVP/ZnO-0.5 (0.5 mmol), PAN/PVP/ZnO-1 (1 mmol), PAN/PVP/ZnO-2 (2 mmol), and PAN/PVP/Zn(NO_3) (2 mmol, without heat treatment), respectively. The PAN/PVP/Zn(NO_3) sample was prepared using the same electrospinning procedure with 2 mmol of $Zn(NO_3)_2 \cdot 6H_2O$ but was not subjected to the heat treatment step, serving as a comparison to evaluate the effect of thermal decomposition on morphology, zinc incorporation, and photocatalytic performance.

2.3 Materials characterization

Nanofiber surface morphology and microstructural features were examined using a scanning electron microscope (SEM, JEOL JSM-6510) equipped with an energy dispersive X-ray spectrometer (EDS) for elemental composition analysis. Prior to imaging, all samples were sputter-coated with a thin layer of gold (Au) to ensure surface conductivity. SEM micrographs were acquired at an accelerating voltage of 15 kV and magnifications of 1000×, 5000×, and 10,000×. Mean fiber diameters were determined from SEM micrographs by measuring at 100 randomly selected individual fibers per sample using ImageJ software (National Institutes of Health, USA). Crystallographic phase analysis was performed by X-ray diffraction (XRD, Rigaku SmartLab SE Basic diffractometer) using Cu Kα radiation (λ = 1.5406 Å) over a 2θ range of 10°–80°. Chemical bonding states and functional group identification were carried out using a Fourier-transform infrared spectrometer (FTIR, IRSpirit, Shimadzu) in attenuated total reflectance (ATR) mode over the wavenumber range of 500–4000 cm^{-1}, enabling evaluation of the PAN/PVP polymer matrix integrity and detection of any structural modifications induced by heat treatment.

2.4 Single pollutant degradation tests

The photocatalytic performance of the PAN/PVP/ZnO nanofiber membranes was evaluated using methylene blue (MB) as a model cationic dye pollutant. In each run, 50 mg of

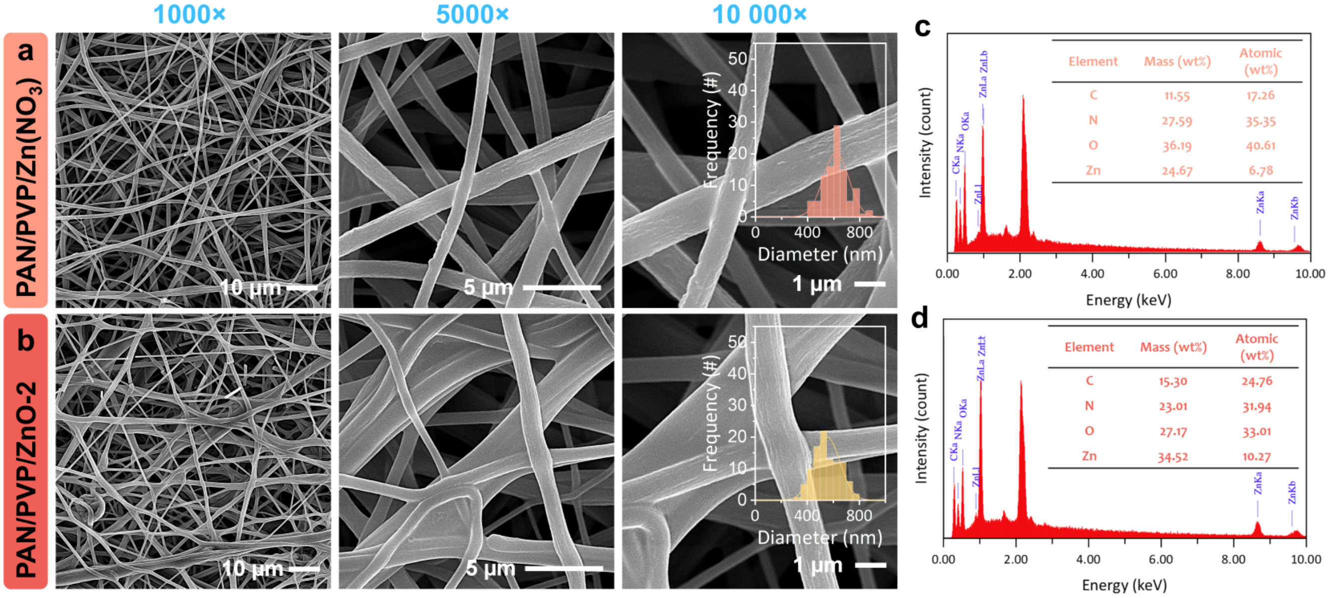

Figure 3. Effect of heat treatment on nanofiber morphology and elemental composition at 2 mmol $Zn(NO_3)_2$ loading. SEM micrographs at 1000×, 5000×, and 10,000× magnifications for (a) PAN/PVP/$Zn(NO_3)_2$ (as-spun, without heat treatment) and (b) PAN/PVP/ZnO-2 (heat-treated at 450 °C under N_2). Corresponding EDS spectra and elemental composition of (c) PAN/PVP/$Zn(NO_3)_2$ and (d) PAN/PVP/ZnO-2.

the nanofiber membrane was immersed in 100 mL of aqueous MB solution (5 mg/L). Photocatalytic degradation was carried out under ultraviolet irradiation supplied by four 10 W Philips TUV germicidal lamps ($\lambda \approx 254$ nm) arranged symmetrically around the reaction vessel for uniform light distribution. Liquid samples of approximately 3 mL were collected at predetermined time intervals (0, 60, 90, 120, 150, and 180 min) and filtered through a syringe membrane filter to separate any suspended particles. The residual MB concentration in each aliquot was measured by UV-Vis absorption spectrophotometry (Shimadzu UV-1200) at the maximum-absorption wavelength of 663 nm.

The normalized concentration ratio (C/C_0) was plotted as a function of irradiation time to compare the degradation performance of all samples, where C_0 denotes the equilibrium concentration at the end of the dark period and C is the MB concentration at irradiation time t. The degradation kinetics were analyzed using the pseudo-first-order Langmuir–Hinshelwood model, expressed as Eq. (1):

$$\ln\left(\frac{C_0}{C}\right) = k\,t \tag{1}$$

where k (min^{-1}) is the apparent rate constant derived from the slope of the linear regression. A mass-normalized rate constant, k_m ($\text{min}^{-1}\ \text{g}^{-1}$), was additionally calculated using Eq. (2) to enable direct comparison of intrinsic catalytic activity:

$$k_m = \frac{k}{m_{\text{catalyst}}} \tag{2}$$

where m_{catalyst} is the mass of the nanofiber membrane catalyst (g). All photocatalytic experiments were conducted under identical conditions to ensure a fair comparison among the samples.

3. RESULTS AND DISCUSSION

3.1 Material and structural characteristics of PAN/PVP/ZnO nanofibers

The surface morphology and microstructure of the electrospun PAN/PVP nanofiber membranes with varying ZnO loadings (0, 0.5, 1, and 2 mmol) were examined by SEM at magnifications of 1000×, 5000×, and 10,000×, as presented in Figure 1. All four samples exhibited continuous, bead-free nanofiber morphology with a randomly oriented, non-woven mat structure, indicating that the electrospinning parameters (9 kV, 0.5 mL/h, 12 cm working distance) were well-optimized for stable jet formation across all solution compositions. The absence of bead defects confirmed that the polymer concentration and solution viscosity were sufficient to sustain continuous fiber stretching under the applied electric field [15,20].

At low magnification (1000×, Figure 1a–d, top row), the PAN/PVP (Figure 1a), PAN/PVP/ZnO-0.5 (Figure 1b), and PAN/PVP/ZnO-1 (Figure 1c) membranes displayed dense, interconnected fibrous networks with open pore structures, which are advantageous for liquid permeation and pollutant accessibility during photocatalytic applications. However, the PAN/PVP/ZnO-2 membrane (Figure 1d) exhibited some broken nanofibers at 1000× magnification, indicating that the excessive ZnO loading compromised the mechanical integrity of the fibers. The fiber breakage at 2 mmol loading can be attributed to the embrittlement of the nanofiber structure caused by the high inorganic content, which disrupts the continuity of the polymer matrix and creates stress concentration points, particularly after the thermal decomposition of $Zn(NO_3)_2$ during heat treatment [21,22].

At higher magnifications (5000× and 10,000×, Figure 1a–d, middle and bottom rows), the individual fiber morphology was more clearly resolved. Quantitative fiber diameter analysis performed using ImageJ software (100 measurements per sample) revealed mean diameters of 404 ±

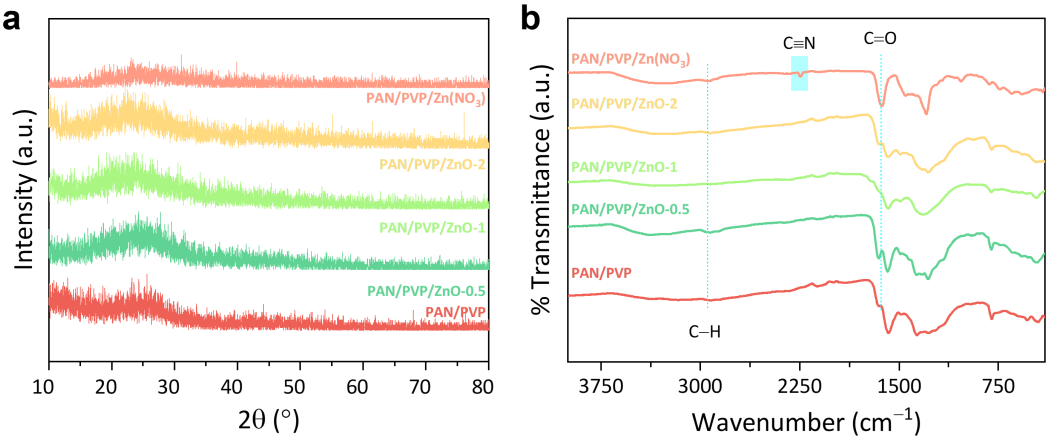

Figure 4. (a) XRD patterns and (b) FTIR spectra of PAN/PVP, PAN/PVP/ZnO-0.5, PAN/PVP/ZnO-1, PAN/PVP/ZnO-2, and PAN/PVP/Zn(NO$_3$)$_2$ nanofiber membranes. Dashed lines in the FTIR spectra indicate the characteristic C≡N stretching (~2240 cm^{-1}) and C=O stretching (~1660 cm^{-1}) absorption bands.

60 nm for PAN/PVP, 362 ± 57 nm for PAN/PVP/ZnO-0.5, 355 ± 51 nm for PAN/PVP/ZnO-1, and 552 ± 99 nm for PAN/PVP/ZnO-2. The neat PAN/PVP nanofibers (Figure 1a) exhibited smooth, cylindrical surfaces. At 0.5 and 1 mmol ZnO loadings (Figure 1b,c), the fiber diameters slightly decreased relative to PAN/PVP, while maintaining smooth surfaces with no visible particle aggregation. The decrease in fiber diameter at low ZnO loadings is attributed to the increased electrical conductivity of the spinning solution from the dissolved Zn(NO$_3$)$_2$ salt, which enhanced the electrostatic stretching force during electrospinning [23,24]. At 2 mmol ZnO loading (Figure 1d), the mean fiber diameter increased to 552 ± 99 nm with a broader distribution, attributed to the higher solution viscosity from the elevated Zn(NO$_3$)$_2$ concentration [23,24].

Notably, no distinct ZnO particle protrusions or surface roughening were observed on the fiber surfaces at any ZnO loading, even at 10,000× magnification. This observation suggests that the ZnO nanocrystals formed via thermal decomposition of Zn(NO$_3$)$_2$ at 450 °C were predominantly embedded within the nanofiber matrix rather than deposited on the surface, or that the crystallite size was below the resolution limit of SEM. This embedded morphology is consistent with the in-situ formation mechanism, where ZnO nucleated and grew within the polymer fiber during heat treatment [25]. The smooth fiber surface morphology across all samples also indicates the absence of large-scale ZnO aggregation, which is beneficial for maintaining high surface area and photocatalytic activity.

Energy dispersive X-ray spectroscopy (EDS) was employed to verify the elemental composition and confirm the successful incorporation of ZnO into the PAN/PVP nanofiber matrix. The EDS spectra and corresponding quantitative elemental analysis for the PAN/PVP (Figure 2a), PAN/PVP/ZnO-0.5 (Figure 2b), PAN/PVP/ZnO-1 (Figure 2c), and PAN/PVP/ZnO-2 (Figure 2d) samples are presented in Figure 2. The EDS spectrum of the neat PAN/PVP nanofibers (Figure 2a) exhibited characteristic peaks corresponding to carbon (C, 22.31 wt%), nitrogen (N, 34.53 wt%), and oxygen (O, 43.16 wt%), which are the constituent elements of the PAN and PVP polymer chains. No zinc signal was detected, confirming the absence of ZnO in the control sample.

Upon ZnO incorporation, characteristic Zn Kα (~8.6 keV) and Zn Kβ (~9.6 keV) peaks emerged in the EDS spectra of all ZnO-loaded samples (Figure 2b–d), providing direct evidence of successful zinc incorporation into the nanofiber matrix. The Zn content increased systematically with increasing ZnO loading: from 11.65 wt% (3.03 at%) at 0.5 mmol, to 19.91 wt% (5.15 at%) at 1 mmol, and further to 34.52 wt% (10.27 at%) at 2 mmol. This progressive and approximately proportional increase in Zn concentration confirmed that the Zn(NO$_3$)$_2$ precursor was effectively retained within the nanofibers during electrospinning and subsequently converted to ZnO during the heat treatment at 450 °C. Concurrently, the carbon content decreased from 22.31 wt% in PAN/PVP to 15.30 wt% in PAN/PVP/ZnO-2, the nitrogen content decreased from 34.53 to 23.01 wt%, and the oxygen content decreased from 43.16 to 27.17 wt%. These reductions are attributed to the dilution effect, as the increasing proportion of ZnO within the nanofiber matrix correspondingly reduces the relative fraction of the polymer-derived elements (C, N, O). The detection of only C, N, O, and Zn across all samples further confirmed the compositional purity of the nanofiber membranes, with no evidence of contamination from the electrospinning or heat treatment process.

To evaluate the role of heat treatment in converting the Zn(NO$_3$)$_2$ precursor into the photocatalytically active ZnO phase, a comparative study was conducted between PAN/PVP/Zn(NO$_3$)$_2$ (as-spun nanofibers without heat treatment) and PAN/PVP/ZnO-2 (heat-treated at 450 °C under N$_2$ atmosphere). Both samples were prepared from the same electrospinning solution containing 2 mmol Zn(NO$_3$)$_2$·6H$_2$O; the only difference was whether the subsequent heat treatment step was applied. Figure 3 presents the SEM micrographs at three magnifications (1000×, 5000×, and 10,000×) and corresponding EDS analysis for both samples.

Both samples exhibited continuous, bead-free nanofiber morphology (Figure 3a,b). The as-spun PAN/PVP/Zn(NO$_3$)$_2$ nanofibers (Figure 3a) appeared relatively thicker with smoother surfaces, as the Zn(NO$_3$)$_2$ remained dissolved within the polymer matrix without undergoing thermal decomposition. In contrast, the heat-treated PAN/PVP/ZnO-2 nanofibers (Figure 3b) exhibited slightly refined fiber morphology, consistent with the structural densification and polymer chain rearrangement induced by the calcination at 450

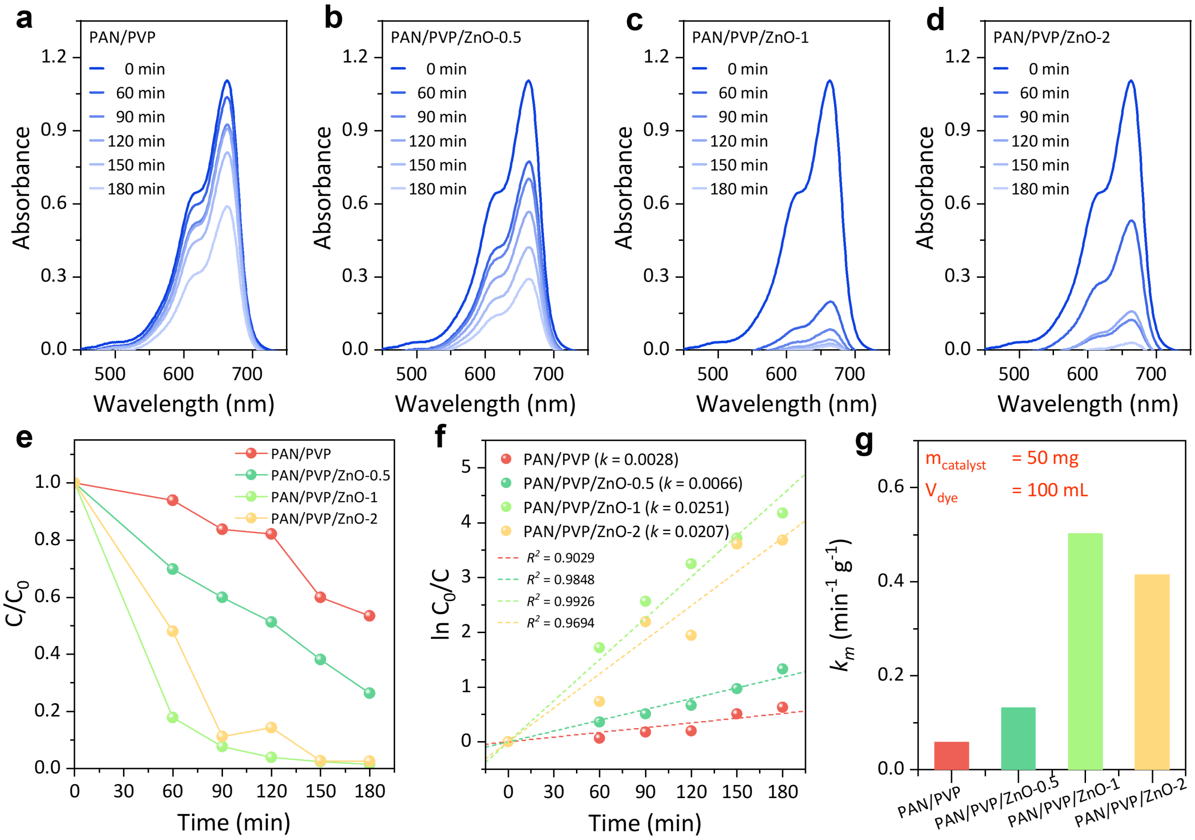

Figure 5. Photocatalytic degradation of MB by PAN/PVP nanofiber membranes with varying ZnO loadings (mcatalyst = 50 mg, V = 100 mL, C_0 = 5 mg L^{-1}). Time-dependent UV-Vis absorption spectra of MB solution in the presence of (a) PAN/PVP, (b) PAN/PVP/ZnO-0.5, (c) PAN/PVP/ZnO-1, and (d) PAN/PVP/ZnO-2. (e) Normalized concentration (C/C_0) as a function of UV irradiation time. (f) Pseudo-first-order kinetic plots of $\ln(C_0/C)$ versus irradiation time with corresponding rate constants (k) and R^2 values. (g) Mass-normalized rate constants (km, min^{-1} g^{-1}) for each sample.

°C [25].

The EDS analysis revealed a notable difference in the apparent zinc content between the two samples. The heat-treated PAN/PVP/ZnO-2 sample contained 34.52 wt% Zn (Figure 3d), whereas the as-spun PAN/PVP/$Zn(NO_3)_2$ sample contained 24.67 wt% Zn (Figure 3c). This difference does not reflect a loss of zinc, but rather the removal of volatile decomposition byproducts during heat treatment. During calcination, $Zn(NO_3)_2$ undergoes thermal decomposition to form ZnO with the release of gaseous NO_2 and O_2 according to the reaction: $2Zn(NO_3)_2 \rightarrow 2ZnO + 4NO_2\uparrow + O_2\uparrow$. The loss of these volatile species reduces the total sample mass, thereby increasing the relative weight fraction of Zn in the remaining nanofiber structure.

This interpretation is further supported by the higher nitrogen content in the as-spun PAN/PVP/$Zn(NO_3)_2$ sample (27.59 vs. 23.01 wt%), which is attributable to the nitrogen from the intact nitrate groups (NO_3^-) that were not yet decomposed. Similarly, the higher oxygen content (36.19 vs. 27.17 wt%) reflects the additional oxygen from the retained nitrate groups. These compositional differences confirm that the heat treatment step is essential for the thermal decomposition of the $Zn(NO_3)_2$ precursor into the photocatalytically active ZnO phase, while simultaneously removing the nitrate byproducts from the nanofiber matrix.

The XRD patterns of all five samples are presented in Figure 4a. The neat PAN/PVP nanofibers exhibited a broad diffraction halo centered at $2\theta \approx 17°$, corresponding to the (100) plane of semi-crystalline PAN [26,27], and a broad hump at $2\theta \approx 22–27°$ from the amorphous PVP component. For all ZnO-loaded samples, the XRD patterns remained similar to neat PAN/PVP without sharp diffraction peaks characteristic of crystalline hexagonal wurtzite ZnO (JCPDS Card No. 36-1451) [28]. The expected ZnO peaks at $2\theta = 31.8°$ (100), 34.4° (002), and 36.3° (101) were not resolved above the amorphous background, which can be attributed to the formation of ultrasmall ZnO nanocrystallites and the low ZnO concentration relative to the dominant polymer matrix. The PAN/PVP/$Zn(NO_3)_2$ sample also displayed a similar amorphous pattern, confirming that no crystalline ZnO phase was formed without heat treatment. Although crystalline ZnO peaks were not detected by XRD, the successful zinc incorporation was confirmed by EDS analysis (Figure 2), and amorphous or nanocrystalline ZnO has been reported to exhibit photocatalytic activity under UV irradiation.

The FTIR spectra of all five samples are presented in Figure 4b. All samples exhibited the characteristic absorption bands of both PAN and PVP: C≡N stretching at ~2240 cm^{-1} (nitrile group of PAN), C=O stretching at ~1660 cm^{-1} (amide carbonyl of PVP), and C–H stretching at 2900–3000 cm^{-1} from the polymer backbones [29,30]. The persistence of these bands across all compositions confirmed that the polymer matrix retained its structural integrity after ZnO incorporation and heat treatment. Subtle decreases in peak intensities with increasing ZnO content were consistent with the dilution of the polymer fraction, corroborating the EDS trends (Figure 2).

3.2 Photocatalytic degradation of methylene blue under UV irradiation

The photocatalytic performance was evaluated by monitoring the UV-Vis absorption spectra of MB solution (characteristic peak at ~664 nm) during UV irradiation at 0, 60, 90, 120, 150, and 180 min (Figure 5a–d). The neat PAN/PVP membrane (Figure 5a) showed only a minimal decrease in absorbance over 180 min, attributed to physical adsorption onto the nanofiber surface. The PAN/PVP/ZnO-0.5 sample (Figure 5b) exhibited a moderate progressive decrease, demonstrating the onset of photocatalytic activity. The PAN/PVP/ZnO-1 sample (Figure 5c) showed the most dramatic decrease, with near-complete disappearance of the MB peak at 150–180 min, indicating highly efficient photocatalytic degradation. The PAN/PVP/ZnO-2 sample (Figure 5d) also showed significant MB degradation, but less pronounced than ZnO-1 despite its higher ZnO content.

The normalized concentration (C/C_0) versus irradiation time is plotted in Figure 5e. The MB removal after 180 min followed the order: PAN/PVP/ZnO-1 (~95%) > PAN/PVP/ZnO-2 (~80%) > PAN/PVP/ZnO-0.5 (~60%) > PAN/PVP (~20%). The neat PAN/PVP removal was attributed to physical adsorption onto the high-surface-area nanofiber membrane. The decline in photocatalytic efficiency at 2 mmol loading, despite the highest ZnO content, may be related to the morphological changes observed at this loading, including the increased fiber diameter, broader size distribution, and fiber breakage revealed by SEM (Figure 1d), which could reduce the effective surface area available for photocatalytic reactions.

The degradation kinetics were analyzed using the pseudo-first-order model: $\ln(C_0/C) = k \cdot t$ (Figure 5f). All samples showed good linear fitting ($R^2 > 0.90$), confirming pseudo-first-order kinetics consistent with the Langmuir–Hinshelwood mechanism [31,32]. The apparent rate constants followed the order: PAN/PVP/ZnO-1 ($k = 0.0251$ min^{-1}, $R^2 = 0.9926$) > PAN/PVP/ZnO-2 ($k = 0.0207$ min^{-1}, $R^2 = 0.9694$) > PAN/PVP/ZnO-0.5 ($k = 0.0066$ min^{-1}, $R^2 = 0.9848$) > PAN/PVP ($k = 0.0028$ min^{-1}, $R^2 = 0.9029$). The rate constant of PAN/PVP/ZnO-1 was approximately 9.0 times higher than that of the neat PAN/PVP membrane. The mass-normalized rate constant ($k_m = k / m_{catalyst}$) was calculated to compare the intrinsic catalytic activity (Figure 5g). PAN/PVP/ZnO-1 exhibited the highest k_m of 0.502 min^{-1} g^{-1}, followed by PAN/PVP/ZnO-2 (0.414 min^{-1} g^{-1}), PAN/PVP/ZnO-0.5 (0.132 min^{-1} g^{-1}), and PAN/PVP (0.056 min^{-1} g^{-1}).

4. CONCLUSIONS

PAN/PVP/ZnO nanofiber membranes were successfully fabricated via electrospinning followed by heat treatment at 450 °C, with ZnO loadings of 0, 0.5, 1, and 2 mmol. SEM revealed continuous, bead-free nanofibers with mean diameters of 355–552 nm, and EDS confirmed systematic Zn incorporation up to 34.52 wt%. The heat treatment step was essential for converting $Zn(NO_3)_2$ into the photocatalytically active ZnO phase, while XRD and FTIR confirmed the retention of the polymer matrix integrity. Among the tested formulations, PAN/PVP/ZnO-1 (1 mmol) achieved the highest MB degradation of ~95% within 180 min ($k = 0.0251$ min^{-1}, $R^2 = 0.9926$), approximately 9 times faster than the neat PAN/PVP membrane. The 1 mmol loading represents optimal formulation, while higher loading (2 mmol) led to reduced photocatalytic performance, which correlated with the degraded fiber morphology observed by SEM at this loading. The PAN/PVP/ZnO-1 nanofiber membrane demonstrates strong potential as a recoverable photocatalyst for dye removal from wastewater. Future studies on reusability, visible-light-driven photocatalysis, and real wastewater application would further advance its practical utility.

FUNDING DECLARATION

This study receives no funding.

DATA AVAILABILITY STATEMENT

The datasets generated during and/or analyzed during the current study are available from the corresponding author on reasonable request.

CONFLICT OF INTEREST

The authors declare that there are no conflicts of interest.

REFERENCES

[1] Aragaw TA. A review of dye biodegradation in textile wastewater, challenges due to wastewater characteristics, and the potential of alkaliphiles. *Journal of Hazardous Materials Advances*. 2024;16:100493. doi:10.1016/j.hazadv.2024.100493.

[2] Al-Tohamy R, Ali SS, Li F, Okasha KM, Mahmoud YA-G, Elsamahy T, Jiao H, Fu Y, Sun J. A critical review on the treatment of dye-containing wastewater: Ecotoxicological and health concerns of textile dyes and possible remediation approaches for environmental safety. *Ecotoxicol. Environ. Saf.*. 2022;231:113160. doi:10.1016/j.ecoenv.2021.113160.

[3] Oladoye PO, Ajiboye TO, Omotola EO, Oyewola OJ. Methylene blue dye: Toxicity and potential elimination technology from wastewater. *Results in Engineering*. 2022;16:100678. doi:10.1016/j.rineng.2022.100678.

[4] Ávila FG, Cabrera-Sumba J, Valdez-Pilataxi S, Villalta-Chungata J, Valdiviezo-Gonzales L, Alegria-Arnedo C. Removal of heavy metals in industrial wastewater using adsorption technology: Efficiency and influencing factors. *Clean. Eng. Technol.*. 2025;24:100879. doi:10.1016/j.clet.2025.100879.

[5] Eniola JO, Kumar R, Barakat MA, Rashid J. A review on conventional and advanced hybrid technologies for pharmaceutical wastewater treatment. *J. Clean. Prod.*. 2022;356:131826. doi:10.1016/j.jclepro.2022.131826.

[6] Khan MD, Singh A, Khan MZ, Tabraiz S, Sheikh J. Current perspectives, recent advancements, and efficiencies of various dye-containing wastewater treatment technologies. *Journal of Water Process Engineering*. 2023;53:103579. doi:10.1016/j.jwpe.2023.103579.

[7] Hong J, Cho K-H, Presser V, Su X. Recent advances in wastewater treatment using semiconductor photocatalysts. *Curr. Opin. Green Sustain. Chem.*. 2022;36:100644. doi:10.1016/j.cogsc.2022.100644.

[8] Iqbal M Ahtasham, Akram S, khalid S, Lal B, Hassan SU, Ashraf R, Kezembayeva G, Mushtaq M, Chinibayeva N, Hosseini-Bandegharaei A. Advanced photocatalysis as a viable and sustainable wastewater treatment process: A comprehensive review. *Environ. Res.*. 2024;253:118947. doi:10.1016/j.envres.2024.118947.

[9] Ray SK, Cho J, Hur J. A critical review on strategies for improving efficiency of BaTiO3-based photocatalysts for wastewater treatment. *J. Environ. Manage.*. 2021;290:112679. doi:10.1016/j.jenvman.2021.112679.

[10] Kanwal F, Javed T, Hussain F, Wasim M, Batool M. Enhanced dye photodegradation through ZnO and ZnO-based

photocatalysts doped with selective transition metals: a review. *Environmental Technology Reviews*. 2024;13:754-793. doi:10.1080/21622515.2024.2426725.

[11] Manikanika, Chopra L, Kumar R. Combustion-synthesized ZnO-CeO2 heterojunctions for advanced photocatalytic dye degradation. *Inorg. Chem. Commun.*. 2024;160:111896. doi:10.1016/j.inoche.2023.111896.

[12] Das M, Ghatak A, Ray P Guha, Stachewicz U. Advancements in ZnO-based photocatalysts for effective rhodamine dye removal from water. *Sustainable Materials and Technologies*. 2024;42:e01138. doi:10.1016/j.susmat.2024.e01138.

[13] Venkatesh G, Palanisamy G, Lee J, Manimaran K, Abu-Yousef I, Kanan S. Synergistic effect of dual Z-scheme ZnO/g-C3N4/V2O5 heterogeneous nanocomposite for photocatalytic decontamination of mixed dye and pharmaceutical drug under visible light irradiation. *J. Alloys Compd.*. 2025;1010:178186. doi:10.1016/j.jallcom.2024.178186.

[14] Meng F, Liu Y, Wang J, Tan X, Sun H, Liu S, Wang S. Temperature dependent photocatalysis of g-C3N4, TiO2 and ZnO: Differences in photoactive mechanism. *J. Colloid Interface Sci.*. 2018;532:321-330. doi:10.1016/j.jcis.2018.07.131.

[15] Li N, Wang W, Zhu L, Cui W, Chen X, Zhang B, Zhang Z. A novel electro-cleanable PAN-ZnO nanofiber membrane with superior water flux and electrocatalytic properties for organic pollutant degradation. *Chemical Engineering Journal*. 2021;421:127857. doi:10.1016/j.cej.2020.127857.

[16] Mohammed MI, Khafagy RM, Hussien MSA, Sakr GB, Ibrahim MA, Yahia IS, Zahran HY. Enhancing the structural, optical, electrical, properties and photocatalytic applications of ZnO/PMMA nanocomposite membranes: towards multifunctional membranes. *Journal of Materials Science: Materials in Electronics*. 2022;33:1977-2002. doi:10.1007/s10854-021-07402-3.

[17] Li Y, Wang Y, Song J, Zheng K, Zhang H, Li J. A recyclable self-supporting flexible ZIF-8@aminated PAN-PVP material for highly selective phosphate removal from wastewater. *Colloids Surf. A Physicochem. Eng. Asp.*. 2025;707:135958. doi:10.1016/j.colsurfa.2024.135958.

[18] Selvam S, Sundrarajan M. Functionalization of cotton fabric with PVP/ZnO nanoparticles for improved reactive dyeability and antibacterial activity. *Carbohydr. Polym.*. 2012;87:1419-1424. doi:10.1016/j.carbpol.2011.09.025.

[19] Suo R, Xie L, Liao J, Chen J, Lu C-Z. Enhanced Charge Separation in a PAN/ZnO Nanocomposite for Promoted Photocatalytic Hydrogen Evolution. *ACS Appl. Energy Mater.*. 2024;7:5668-5678. doi:10.1021/acsaem.4c00521.

[20] Hartati S, Zulfi A, Maulida PYD, Yudhowijoyo A, Dioktyanto M, Saputro KE, Noviyanto A, Rochman NT. Synthesis of Electrospun PAN/TiO2/Ag Nanofibers Membrane As Potential Air Filtration Media with Photocatalytic Activity. *ACS Omega*. 2022;7:10516-10525. doi:10.1021/acsomega.2c00015.

[21] Wei T, Li W, Zhang J, Xie X. Synthesis of Tb2O3/ZnO composite nanofibers via electrospinning as chemiresistive gas sensor for detecting NO gas. *J. Alloys Compd.*. 2023;947:169651. doi:10.1016/j.jallcom.2023.169651.

[22] Ersöz E, Yildirim O Altintas. Green synthesis and characterization of Ag-doped ZnO nanofibers for photodegradation of MB, RhB and MO dye molecules. *Journal of the Korean Ceramic Society*. 2022;59:655-670. doi:10.1007/s43207-022-00202-3.

[23] Moezzi M, Moghaddam MK, Rahimzadeh J, Ranjbar-Mohammadi M, Barez F. Investigation of PLA/ZnO nanofibers for piezoelectric and nerve regeneration applications. *Sens. Actuators A Phys.*. 2025;386:116340. doi:10.1016/j.sna.2025.116340.

[24] Gao H, Joshi B, Samuel E, Khadka A, Kim S Wung, Aldalbahi A, El-Newehy M, Yoon SS. Freestanding electrodes based on nitrogen-doped carbon nanofibers and zeolitic imidazolate framework-derived ZnO for flexible supercapacitors. *Appl. Surf. Sci.*. 2024;651:159221. doi:10.1016/j.apsusc.2023.159221.

[25] Yin R, Li Y, Li W, Gao F, Chen X, Li T, Liang J, Zhang H, Gao H, Li P, Zhou Y. High-temperature flexible electric Piezo/pyroelectric bifunctional sensor with excellent output performance based on thermal-cyclized electrospun PAN/Zn(Ac)2 nanofiber mat. *Nano Energy*. 2024;124:109488. doi:10.1016/j.nanoen.2024.109488.

[26] Kim J-G, Kim H-C, Kim ND, Khil M-S. N-doped hierarchical porous hollow carbon nanofibers based on PAN/PVP@SAN structure for high performance supercapacitor. *Compos. B Eng.*. 2020;186:107825. doi:10.1016/j.compositesb.2020.107825.

[27] Ebrahimi F, Nabavi SR, Omrani A. Fabrication of hydrophilic special sandwich structure of PAN/GO/SiO2 electrospun membrane decorated with SiO2 nanoparticles for oil/water separation. *Journal of Water Process Engineering*. 2022;48:102926. doi:10.1016/j.jwpe.2022.102926.

[28] Khan MGI, Nurfitria R, Anggraini T, Aini Q, Hanifah IR, Nurfani E, Aflaha R, Triyana K, Taher T, Rianjanu A. Hydrothermal synthesis of CeO2/ZnO heterojunctions for effective photocatalytic degradation of organic pollutants. *Materials Science and Engineering: B*. 2025;322:118630. doi:10.1016/j.mseb.2025.118630.

[29] Wu H, Wang Y, Zhang X, Xing W, Li L, Wang H, Huang L, Tang J. PAN/ CB spheres modified PAN/PVP dual amphiphilic porous nanofiber membranes for high-performance oil-water separation. *Colloids Surf. A Physicochem. Eng. Asp.*. 2025;726:137768. doi:10.1016/j.colsurfa.2025.137768.

[30] Geng Y, Zhang P, Wang Q, Liu Y, Pan K. Novel PAN/PVP Janus ultrafine fiber membrane and its application for biphasic drug release. *J. Mater. Chem. B*. 2017;5:5390-5396. doi:10.1039/C7TB00929A.

[31] Wu H, Li L, Wang S, Zhu N, Li Z, Zhao L, Wang Y. Recent advances of semiconductor photocatalysis for water pollutant treatment: mechanisms, materials and applications. *Physical Chemistry Chemical Physics*. 2023;25:25899-25924. doi:10.1039/D3CP03391K.

[32] Swaminaathan P, Saravanan A, Yaashikaa PR, Vickram AS. Recent advances in photocatalytic degradation of persistent organic pollutants: Mechanisms, challenges, and modification strategies. *Sustainable Chemistry for the Environment*. 2024;8:100171. doi:10.1016/j.scenv.2024.100171.